

1 **CO₂ air-sea disequilibrium and preformed Alkalinity in the Pacific and Indian oceans**
2 **calculated from Subsurface Layer data**

3 Paula C. Pardo^{a*}, Marcos Vázquez-Rodríguez^a, Fiz F. Pérez^a and Aida F. Rios^a.

4 ^aInstituto de Investigaciones Marinas, CSIC, Eduardo Cabello 6, E-36208 Vigo, Spain.
5 pconde@iim.csic.es; mvazquez@iim.csic.es; fiz.perez@iim.csic.es; aida@iim.csic.es

6 *Corresponding author: pconde@iim.csic.es, Tel.: +34 986 231930 Ext. 374. Fax: +34 986 292762

7

8 **Abstract**

9 This work estimates new regionalized empirical parameterizations for preformed alkalinity (A_T°) and
10 the CO₂ air-sea disequilibrium (ΔC_{dis}). Both are key terms for the computation of anthropogenic CO₂
11 in the back-calculation methods. Data from the subsurface layer (75–180m depth range) covering an
12 area from North to South and from 19°E to 67.5°W (Pacific and Indian oceans) were taken from
13 GLODAP (The Global Ocean Data Analysis Project) database. The subsurface layer is proved as a
14 reliable reference for representing the main characteristics of the different water masses of the
15 oceans. Besides, handling data from the two ocean basins altogether makes the new parameterizations
16 of A_T° and ΔC_{dis} to be more globally consistent. Nevertheless, each ocean basin, at least in some
17 regions, has different oceanographic characteristics based on its proper dynamical processes and
18 water masses formation. In order to maintain each ocean basin ‘identity’ the whole domain was
19 divided in six different regions (two of them sharing waters from Pacific and Indian oceans) and
20 parameterizations in each region for both terms were obtained. Previously, data were transformed
21 into a grid of 4°lat. x 5°lon. and the results obtained from the parameterizations were visualized and
22 compare with pCO₂ climatologies. From the comparisons with previous ΔC_{dis} estimations good
23 results are obtained showing the reliability and robustness of the new regionalized empiric
24 parameterizations.

25

1 **Keywords**

2 Alkalinity, Parameterization, Air-water exchanges, Carbon cycle, Carbon sinks, Indian Ocean,
3 Pacific Ocean, Water masses

4

5 **1. Introduction**

6 The current increase of atmospheric CO₂ levels and their impact on rising global temperatures and
7 climate change is one of the foremost concerns and high-priority issues for policymakers and
8 scientists nowadays. Although the percentage of anthropogenic CO₂ uptake by the ocean sink with
9 respect to the total CO₂ emissions is decreasing during this decade (Le Quéré et al. 2009), one third
10 of the total anthropogenic CO₂ inventory is stored in the oceans (Sabine et al., 2004). The Pacific
11 Ocean represents nearly half of the global ocean's volume and is thus a crucial water body for the
12 accurate assessment of the global oceanic uptake of anthropogenic CO₂ (C_{ANT}). Sabine et al. (2002;
13 hereinafter S'02) estimated the Pacific inventory of C_{ANT} to be 44.5 ± 5 PgC for the nominal year
14 1994. The abundance of very old deep waters and the lack of deep-water formation in the North
15 Pacific basin (Schmitz, 1996) make this ocean to be a relatively small sink of C_{ANT} compared with
16 the Atlantic Ocean (Sabine et al., 2004). The Indian Ocean behaves similarly in this regard, and has a
17 total C_{ANT} inventory of 20.3 ± 3 PgC in 1995 (Sabine et al, 1999; hereinafter S'99), i.e., about half
18 that of the Pacific Ocean.

19 One of the most widespread techniques to estimate the C_{ANT} fraction of the total inorganic carbon
20 (C_T) in seawater is that of back-calculation methods (Brewer, 1978; Chen and Millero, 1979;
21 Wallace, 2001). Back-calculation methods strive to remove from C_T measurements the
22 biogeochemical changes undergone in different water masses since they were last in contact with the
23 atmosphere, i.e., when they outcrop, at the time of water mass formation (WMF). These techniques
24 are subjected to uncertainties and approximations, leaving plenty of room for improvement (Gruber
25 et al., 1996; hereinafter GSS'96; Körtzinger et al., 1998; Pérez et al., 2002; Lo Monaco et al., 2005;

1 Vázquez-Rodríguez et al., 2009a). All these techniques need to estimate the preformed alkalinity and
2 C_T terms (A_T° , C_T°) of reference (i.e., the A_T and C_T that a given water mass has when last in contact
3 with the atmosphere), and the way these terms are calculated largely determines the differences
4 found between methods. The technique utilized in GSS'96 (the ΔC^* method) introduced for the first
5 time in the context of back-calculation methods the CO_2 air-sea disequilibrium term (ΔC_{dis}), which,
6 by definition, is established at the time of WMF, assuming that other gases (O_2 and CFCs) are
7 saturated. The A_T° and ΔC_{dis} are critical terms when back-calculating C_{ANT} , and they should be
8 obtained to the highest possible degree of accuracy (Matsumoto and Gruber, 2005). The use of high-
9 quality datasets and some specific techniques (developed in this work) should largely help reducing
10 biases and yield robust parameterizations for the afore-mentioned two terms.

11 Over the 1990s, a compendium of data from the WOCE/JGOFS/OACES cruises was put together in
12 an oceanographic database thanks to the cooperative effort of different international entities inside
13 the Global Ocean Data Analysis Project (GLODAP;
14 http://cdiac.ornl.gov/oceans/glodap/Glodap_home.html). All data were merged into a common
15 format set and subjected to rigorous quality control procedures to eliminate systematic data
16 measurement biases (Key et al., 2004). The Indian and Pacific oceans data (Fig. 1a) here used have
17 been collected from a total of 67 cruises (46 cruises from 1985 to 1999 for the Pacific Ocean and 21
18 cruises from 1993 to 1996 for the Indian Ocean) together with historical data (years 1973, 1974,
19 1984, 1987 and 1990 for the Pacific Ocean and years 1977, 1978 and from 1985 to 1987 for the
20 Indian Ocean).

21 This work merges three different approaches to achieve optimised parameterizations of A_T° and ΔC_{dis} .
22 In the first place, the data from the subsurface layer is considered as a reliable reference for
23 preformed properties, irrespective of the sampling date (Vázquez-Rodríguez, 2008). Unlike in the
24 case of surface data, the subsurface layer avoids to a great extent the large seasonal variability of
25 physical-chemical parameters that are usually required in the target parameterizations. On the other

1 hand, this study aims at regionalizing the obtained empiric equations instead of searching for unique
2 global parameterizations of A_T° and ΔC_{dis} . This will be achieved by taking into account the particular
3 dynamics and, especially, the class of water masses formed, so that different regions can be soundly
4 established within each ocean basin. Lastly, the selected dataset will be averaged in $4^\circ\text{lat.} \times 5^\circ\text{lon.}$
5 cells ($4^\circ \times 5^\circ$ grid) in order to minimize the local spatial scale variability and the associated noises
6 generated from the different analytical sources of the A_T and C_T data.

7 Once the set of regionalized empirical parameterizations are obtained, the values of A_T° and ΔC_{dis} will
8 be discussed in detail and compared with previous estimates in each of the considered ocean basins:
9 The A_T° will be compared directly with the subsurface measured alkalinity and with previous
10 parameterizations (GSS'96; S'99; S'02). Also, values of ΔC_{dis} computed from the pCO_2 atlas of
11 Takahashi (Takahashi et al., 2009) will be included in the comparison.

12

13 **2. Methodology and data**

14 **2.1. The subsurface layer reference**

15 The seasonal cycle of the surface layer is reflected by the strong variability of either non-
16 conservative (C_T or pCO_2) or conservative (T , S , $\text{NO} = r_{\text{O/N}}\text{NO}_3 + \text{O}_2$, $\text{PO} = r_{\text{O/P}}\text{PO}_4 + \text{O}_2$, where
17 $r_{\text{O/N}}$ and $r_{\text{O/P}}$ are the stoichiometric coefficients; Broecker, 1974) tracers. Also, the large variability
18 of the short scale processes of physical mixing, thermodynamics and biological activity has an effect
19 on the surface water pCO_2 , thus affecting the ΔC_{dis} and ΔpCO_2 (sea-to-air pCO_2 difference).
20 Although CO_2 air-sea exchange is a surface event, the high variability of the surface layer does not
21 provide the best source of data to estimate preformed variables or ΔC_{dis} (Lo Monaco et al., 2005;
22 Vázquez-Rodríguez et al., 2009a). Different studies have shown that the properties of surface layers
23 of the ocean can only be comparable with those from the lower layers in late wintertime, when WMF
24 occurs and maximum depths of the winter mixed layer (WML) are reached (Woods, 1985; Doney
25 and Jenkins., 1988; Marshall and Schott, 1999; Wallace, 2001; Vázquez-Rodríguez, 2008). The

1 adverse weather conditions in this period of time hamper cruises to be carried, in the high latitudes,
2 and most data sampled are taken typically during spring and summertime (Rodgers et al, 2008).
3 Some previous studies dealing with back-calculation methods have used surface data in their
4 parameterizations of A_T° (GSS'96; Gruber, 1998; Lo Monaco et al., 2005; Levine et al., 2008).
5 However, they discarded that very same surface, euphotic layer data (down to 50/100m and deeper at
6 times) when actually applying their parameterizations to calculate C_{ANT} . Later works (Pérez et al.,
7 2002; Ríos et al., 2003) considered the layer between 50-200m as the best approximation of the
8 WML. Vázquez-Rodríguez (2008) provided solid evidence and proof for the ability of the subsurface
9 layer (100-200m) to retain the biogeochemical properties of a water mass up to six months after the
10 late wintertime formation period. At this moment the preformed properties and the degree of ΔC_{dis}
11 are established at the break-up of the seasonal thermocline and the renewal of water properties are
12 just restarting in the annual cycle.

13 Most of the above-mentioned back-calculation studies were carried out specifically for the Atlantic
14 Ocean, except for those by Lo Monaco et al. (2005), who used data from the Indian-Atlantic
15 boundary, and by Levine et al. (2008), that applied back-calculation methods to carbon-climate
16 model output data. Some examinations were therefore performed here for the Pacific and Indian
17 oceans in order to prove whether or not the hypothesis of the subsurface layer reference applies to the
18 rest of major ocean basins.

19 Here, the subsurface layer between 75m and 180m has been selected, out of several depth-ranges
20 tried, as the one that encompasses best the thermohaline variability of the two basins. Also, this layer
21 is far away enough from the surface not to be influenced by the short-term variability of the
22 uppermost layers and yet can gather (i.e., is affected) the more significant, longer-term variability of
23 the tracers from the winter mixed layer. The T/S diagrams for the Pacific and Indian Oceans are
24 presented in Figure 2 separately. The thermohaline variability of the water column ($Z > 200m$) for
25 the Pacific and Indian oceans constructed with GLODAP bottle data is shown (blue dots). Two

1 additional subsets of GLODAP data were represented in each T/S diagram, i.e., surface ($Z < 25\text{m}$)
2 (green dots) and subsurface layer (red dots) data. Both subsets of data have been averaged to the
3 same $4^\circ \times 5^\circ$ grid. The main two branches of Central Pacific waters (Fig. 2a) and also waters from
4 higher latitudes (Subarctic and Intermediate North Pacific waters) with low potential temperature are
5 well described within the data cluster of the deep layers ($Z > 200\text{m}$). Data from the uppermost 25m
6 are, in general, much more scattered and almost randomly distributed in the T/S space. Most of these
7 surface samples are located in the temperature domains below 3°C and above 18°C . Also, the region
8 of higher salinities ($S > 36$) over the branch of South Pacific Central waters is poorly represented.
9 The subsurface layer data show a quite homogeneous distribution and gather the general
10 thermohaline variability of the water column. The Central Pacific waters are well represented by this
11 dataset and the properties of cold waters are also closer to those of deep waters. The only T/S
12 signature that escapes the wrapping of subsurface data is the signal of the North Atlantic Deep Water
13 (NADW) in the deep waters of the Pacific Ocean.

14 Very similar conclusions are drawn from the T/S diagram for the Indian Ocean basin (Fig. 2b, blue
15 dots). The thermohaline variability of waters below 200 m is dominated by the Indian Central Water
16 ($5^\circ\text{C} \leq \theta \leq 18^\circ\text{C}$) except for a remarkable signal with high salinities ($S > 36$) that comes from the
17 influence of the Red Sea Water outflow. Surface layer datapoints (green dots) are mainly distributed
18 in regions of higher and lower potential temperatures ($\theta < 3^\circ\text{C}$ and $\theta > 18^\circ\text{C}$) and are not at all
19 representative of the water column's thermohaline variability. On the contrary, the distribution of
20 subsurface layer data points is closer to, consistent and descriptive of the thermohaline properties of
21 the water column (red dots). In conclusion, most of the thermohaline variability of the Pacific and
22 Indian Oceans is enclosed better by the T/S distribution of the selected subsurface layer than that
23 showed by surface layer data. The only gap to fill in this last set of data is the distribution of water
24 masses coming from the Red Sea.

25

1 **2.2. Regions**

2 The dynamical behaviour of the different zones of the two ocean basins has been considered when
3 dividing the domain under study in six major regions, with the purpose of obtaining more robust
4 regional and, ultimately, basin-wide parameterizations (Fig. 1b, Table 1). The determination of the
5 latitudinal boundaries of these regions was based on oceanic features, such as common thermohaline
6 properties and circulation patterns (Schmitz, 1996; Tomczak and Godfrey, 2001). A brief description
7 of the regions is provided next.

8

9 **2.2.1. Subarctic Pacific region (*SAP*).**

10 The *SAP* region corresponds to the North Pacific Ocean, north of 45°N. This is a region with low
11 values of potential temperature ($\theta < 5^{\circ}\text{C}$) and salinity ($S < 34.0$) due to its location close to the Arctic
12 Ocean and to the influence of the Subarctic Current. The North Pacific Intermediate Water (NPIW)
13 formation [$33.8 < S < 34.0$; $\theta < 5^{\circ}\text{C}$] takes place in this area.

14

15 **2.2.2. North-Subtropical Pacific region (*NSTP*).**

16 The *NSTP* region encloses the zone of the Pacific Ocean between 25°N and 45°N, which is partly
17 influenced by the strong subtropical gyre including the Kuroshio and the North Pacific currents. This
18 is the formation area of the North Pacific Central Water (NPCW) and displays salinity and θ ranges
19 between 34.0 and 35.2 and 5°C up to 20°C, respectively.

20

21 **2.2.3. Equatorial Pacific region (*EqP*).**

22 The *EqP* region is located in the Pacific Ocean between 15°S and 25°N. The salinity range in this
23 zone goes from 35.0 to 36.0 approximately (Table 1). Surface temperatures reach the maximum in
24 the west side ($\theta > 20^{\circ}\text{C}$) but they drop eastwards to almost 15°C. This region features the most

1 productive coastal upwelling system of the world ocean, associated with the Humboldt Current and
2 where the Equatorial divergence causes very high surface pCO₂ (Takahashi et al. 2009).

3

4 **2.2.4. Equatorial Indian region (*EqI*).**

5 The *EqI* region is located north of 25°N in the Indian Ocean and has very similar features to the *EqP*
6 region. The *EqI* region is an upwelling zone affected by the seasonal monsoon cycle with high
7 surface temperatures ($\theta > 18^{\circ}\text{C}$) and salinity values ranging from 34.9 to 36.3 due to the strong
8 influence of the river plume from the Bay of Bengal and to the salty contributions from the Arabian
9 Sea. The different range in salinities (the northern Indian Ocean is included in this region) compared
10 to that of *EqP* and the not so intense upwelling events in this region of the Indian Ocean suggest
11 considering the *EqI* region separately from the *EqP* region.

12

13 **2.2.5. South Subtropical Indo-Pacific region (*SSTIP*).**

14 The *SSTIP* region is defined jointly for both the Indian and Pacific oceans basins in terms of
15 equations, but with different limits for the Pacific and Indian oceans. In the Indian Ocean the
16 latitudinal limits go from 25°S to 50°S while for the Pacific Ocean it spans from 15°S down to 54°S.
17 Both regions include the subtropical gyres in each of the basins and the formation zones of the South
18 Pacific Central Water (SPCW) and the Indian Central Water (ICW), respectively. Salinity and θ
19 ranges for both SPCW and ICW are very similar, namely: $[34.2 < S < 36.0; 5^{\circ}\text{C} < \theta < 22^{\circ}\text{C}]$ and
20 $[34.0 < S < 35.6; 5^{\circ}\text{C} < \theta < 18^{\circ}\text{C}]$, respectively. In spite of the number of varieties of Central Water
21 along the south subtropical region (Tomczak and Godfrey, 2001), the similarities obtained in the
22 empirical parameterizations for A_T° and ΔC_{dis} (section 3) in both ocean basins make possible to study
23 them as a whole, only subject to minor specific differences in the parameterizations (Table 2).

24

25 **2.2.6. Antarctic Indo-Pacific region (*AAIP*).**

1 The *AAIP* region comprises the Pacific and Indian sectors of the Southern Ocean, where the densest
2 water masses form. The water masses formed in this region enter all three major ocean basins
3 propelled by the strong and turbulent Antarctic Circumpolar Current (ACC) flowing eastwards. The
4 Pacific and Indian boundaries of the *AAIP* region have been established on the basis of surface
5 temperatures ($\theta < 5^{\circ}\text{C}$), namely: south of 50°S for the Indian Ocean basin (19°E - 148°E) and south of
6 54°S in the Pacific Ocean basin (148°E - 67.5°W). The proposed limits match coarsely the
7 Subantarctic Front (SAF), which is a real physical boundary between the high-salinity subtropical
8 gyre waters and the low salinity Antarctic waters. The cooling in surface and ice-free waters nearby
9 the continental shelf region contributes to the WMF of the Ross Sea Water (RSW) that later mixes
10 with the Weddell Sea Water (WSW) and the Circumpolar Deep Water (CDW), which ultimately
11 ends up as Antarctic Bottom Water (AABW; $\theta \approx 0^{\circ}\text{C}$ and $S \approx 34.7$). The circumpolar current also
12 conveys the Antarctic Intermediate Water (AAIW; $3.0^{\circ}\text{C} < \theta < 3.5^{\circ}\text{C}$ and $34.1 < S < 34.2$) to both
13 the Pacific and Indian basins.

14

15 **2.3. The A_{T}° and ΔC_{dis} terms**

16 **2.3.1. A_{T}°**

17 The relevance of the A_{T}° term in the C_{ANT} back-calculation context comes from its involvement in the
18 estimation of CaCO_3 dissolution, which is one of the processes affecting the content of CT once the
19 water masses outcrop from the surface. Under the assumption that A_{T} is not affected by C_{ANT} and,
20 thus, constant over time, the A_{T}° term can be estimated linearly as a function of conservative
21 properties from contemporary water masses. For instance, GSS'96 defined a global expression
22 for A_{T}° using surface data ($Z < 100\text{m}$) of S and the conservative tracer PO ($\text{PO} = 170 * \text{PO}_4 + \text{O}_2$,
23 Anderson and Sarmiento, 1994) via a multiple linear regression (MLR) fit ($A_{\text{T}}^{\circ} = 367.5 + 54.9 * S +$
24 $0.074 * \text{PO}$). Later on time, S'99 calculated a new A_{T}° equation for the Indian Ocean with data from
25 the upper 60m layer that included θ as an additional independent variable ($A_{\text{T}}^{\circ} = 378.1 + 55.22 *$

1 $S + 0.0716 * PO - 1.236 * \theta$). Incorporating θ aimed at fitting changes in alkalinity that the global
 2 equation from GSS'96 could not account for. The A_T° term was also estimated in the Pacific Ocean in
 3 the work from S'02 ($A_T^\circ = 148.7 + 61.36 * S + 0.0941 * PO - 0.582 * \theta$), who used surface data (Z
 4 $< 60\text{m}$) and provided yet another fit that also used S , PO and θ as independent variables. The search
 5 for an ever more elaborated, basin-wide empiric parameterization of the A_T° term is an ongoing
 6 research process (Matsumoto and Gruber, 2005) that is broached in the present work.

7

8 **2.3.2. ΔC_{dis}**

9 The classic ΔC^* method to estimate C_{ANT} inventories (GSS'96) has been widely accepted, applied to
 10 all three major oceanic basins and used in the GLODAP database. The ΔC^* method emerged from an
 11 attempt to separate the C_{ANT} signal from measured C_T values. The first approaches (Brewer, 1978;
 12 Chen and Millero, 1979) estimated C_{ANT} as the C_T concentration difference between current and
 13 preindustrial conditions and providing a general expression to calculate it, namely:

$$14 \quad C_{\text{ANT}} = C_T - C_{T \text{ eq}}^\circ - \Delta C_{\text{bio}} \quad (1)$$

15 where C_T stands for the observed total inorganic carbon, $C_{T \text{ eq}}^\circ$ is the equilibrium C_T concentration for
 16 a preindustrial atmosphere (280 ppm), and ΔC_{bio} is the change in C_T due to remineralization of
 17 organic matter (ROM) and dissolution of calcium carbonate (CaCO_3).

18 GSS'96 added a term to this equation (ΔC_{dis}^*) to account for the CO_2 air-sea disequilibrium of a water
 19 parcel, which is established at the moment the water mass outcrops from the surface, Equation 1
 20 evolved then into:

$$21 \quad C_{\text{ANT}} = \Delta C^* - \Delta C_{\text{dis}}^* \quad (2)$$

22 where ΔC^* equals C_{ANT} in equation 1.

23 Following GSS'96 notation, S'99 defined de ΔC^* term as follows:

$$24 \quad \Delta C^* = C_T - C_{T \text{ eq}}^\circ - r_{\text{C/O}} * \text{AOU} - \frac{1}{2} (A_T - A_T^\circ + r_{\text{N/O}} * \text{AOU}) + r_{\text{C/N}} * N^* \quad (3)$$

1 where $AOU = O_{2\text{ sat}}^{\circ} - O_2$, the third and fourth terms (ΔC_{bio} in equation 1) account for ROM and the
 2 dissolution of CaCO_3 , respectively, N^* is the term involving the denitrification signal introduced by
 3 S'99 and $r_{C/O} = 117/170$, $r_{N/O} = 16/170$ and $r_{C/N} = 106/104$ are the stoichiometric coefficients
 4 (Anderson and Sarmiento, 1994; Gruber and Sarmiento, 1997) . The implicit assumptions here are
 5 that the stoichiometric ratios ($r_{x/y}$) of ROM, dissolution of CaCO_3 and denitrification are constant;
 6 that the preformed concentration of O_2 is given by the O_2 saturation ($O_{2\text{ sat}}^{\circ}$) and that A_T° is invariant
 7 over time. The various assumptions and approximations made in this method lead to known biases in
 8 the estimation of C_{ANT} inventories (Matsumoto and Gruber, 2005).

9 So, as Matsumoto and Gruber (2005) stated: “*the crux of the ΔC^* method is to accurately estimate*
 10 *ΔC_{dis} ” . This term equals ΔC^* (equation 3) in the case of waters that are assumed to contain no
 11 anthropogenic CO_2 . On the contrary, when waters are likely to be affected by C_{ANT} (like the
 12 subsurface layer) the ΔC_{dis} is computed from equation 2 as:*

$$13 \quad \Delta C_{\text{dis}}^* = \Delta C^* - C_{\text{ANT}} \quad (4)$$

14 In order to obtain ΔC_{dis}^* (equation 4) it is then necessary to have an alternative and reliable C_{ANT}
 15 estimate. In GSS'96, C_{ANT} was calculated in these cases using CFCs as tracers to estimate the age of
 16 the water masses. This “shortcut” method (Thomas and Ittekkot, 2001) assumes that there is no
 17 mixing in the ocean interior, only advective transport. Thus, the measured interior tracer
 18 concentration is related to the surface history of the tracer through a simple time lag. Instead of
 19 applying this “shortcut” method, in our work we have used C_{ANT} estimates obtained with the
 20 Transient Time Distribution (TTD) method ($C_{\text{ANT}}^{\text{TTD}}$; Waugh et al., 2006) that are available in the
 21 GLODAP database. The TTD method is more realistic than the shortcut method because it considers
 22 the mixing processes in the distribution of tracers in seawater. In the presence of mixing, there is a
 23 multiplicity of pathways that connect the ocean surface to an interior point, i.e., a probability
 24 distribution of transient times or “transient time distribution”. Importantly, the TTD method avoids

1 one of the main caveats of the shortcut method, which has to do with the overestimation of C_{ANT} at
2 low CFC concentrations, i.e., in “old” water masses (Matear and McNeil, 2003).

3 There exists yet an alternative way to estimate ΔC_{dis} by using the gradient of pCO_2 between the
4 ocean and the atmosphere during late wintertime months, when WMF processes abound. From these
5 data of pCO_2 disequilibria, ΔC_{dis} can be obtained from the following equation:

$$6 \quad \Delta C_{dis} = C_{T\ eq}(pCO_{2sw}) - C_{T\ eq}(pCO_{2atm}) \quad (5)$$

7 where $C_{T\ eq}(pCO_{2sw})$ refers to the saturation concentration of C_T at the observed seawater’s pCO_2
8 (pCO_{2sw}), and $C_{T\ eq}(pCO_{2atm})$ refers to the theoretical surface C_T equilibrated with the atmosphere,
9 both of them calculated from the thermodynamic relationships of the carbon system.

10 The ΔC_{dis} calculated from equation 5 can be denoted as ‘pure’ C_T° disequilibrium, while the ΔC_{dis} in
11 GSS’96, S’99 and S’02 has associated equilibria different from that of purely CO_2 (like O_2 and
12 CFCs; equation 4) and thus infers into the ΔC_{dis} estimate many of the biases associated with the
13 assumptions from the ΔC^* method.

14 Here we present a new approximation to the calculation of ΔC_{dis} that involves MLR fitting, similarly
15 to what is done for the A_T° term, thus avoiding the above-mentioned implicit biases. The ΔC_{dis} here
16 obtained values will be discussed and compared with the ΔC_{dis}^* values from GSS’96 and with those
17 from the methodology applied in S’99 and S’02 (both of them based on the GSS’96 approach).
18 Furthermore, a comparison will be also done with the values obtained through equation 5, based on
19 the pCO_2 data from the Takahashi et al. (2009) climatology.

20

21 **3. Results and discussion**

22 **3.1. Parameterization of A_T°**

23 In order to look for better empiric parameterizations of A_T° a new MLR fit was applied to the
24 described subsurface dataset distributed according to the $4^\circ \times 5^\circ$ grid and separately for each of the six
25 regions (Table 1). Salinity, which is highly correlated with alkalinity through the bicarbonate

1 concentration (Brewer and Goldman., 1976; Millero et al., 1998b), is the main explanatory variable
2 considered in the fit. In order to account for the regional variability of A_T° , θ and PO ($PO = 170 * PO_4 + O_2$)
3 are considered in addition (Chen and Pytkowicz, 1979; Chen, 1990; GSS'96; Millero et
4 al., 1998b; S'99; S'02). The different parameterizations for the six regions were computed with
5 overlapping limits ($\pm 5^\circ$ of latitude) in order to avoid sharp truncations between regions and aim for
6 smoother transitions. The different MLRs obtained and their associated uncertainties are summarized
7 in Table 2. A minor difference in the obtained fit coefficient for θ has been found between oceans in
8 the case of the *SSTIP* region due to the different water mass characteristics (Table 2). The
9 uncertainties of the parameterization are given through the standard error of estimates (*SEE*; Table
10 2), i.e., an estimation of the standard deviation of the residual values. In general, these uncertainties
11 are low and very similar for all the regions. The uncertainties of the A_T° estimates for the Indian and
12 Pacific oceans altogether are of $\pm 5.2 \mu\text{molkg}^{-1}$.

13 The distributions of measured alkalinity, new computed A_T° and residuals are shown in Figure 3.
14 These distributions and the uncertainties in Table 2 show how accurately the set of A_T° equations
15 proposed fit the distribution of measured alkalinity. The highest values of A_T° are located in the
16 *SSTIP* region, mainly in the Pacific basin (Figs. 3a,b). Relatively high values are located north of the
17 *EqI* region due to the influence of the Arabian Sea basin (high salinity) and also near the coast in the
18 *AAIP* region. The lowest values are located in the east part of the *SAP* region and relative minimum
19 values are found in the south-east of the *SSTIP* region, in the Pacific basin. Even though some
20 structures of local processes exist in the distributions shown (e.g. upwelling zones), the residuals
21 appear to be randomly distributed (Fig. 3c) being $\pm 5 \mu\text{molkg}^{-1}$ the most frequent residuals interval
22 found coincident with the *SEE* for the whole domain . The new parameterizations were also applied
23 to the “non-gridded” bottle dataset (Fig. 1a) for the whole domain. The resulting uncertainties were
24 of $\pm 6.2 \mu\text{molkg}^{-1}$ ($n = 6380$).

1 The results of A_T° here obtained were then compared with the previous parameterizations of A_T° from
2 GSS'96, S'99 and S'02 (Fig. 4). In the Pacific Ocean (Fig. 4a), results are in good agreement with all
3 three parameterizations. However, the uncertainties here obtained are considerably lower ($SEE = \pm$
4 $5.5 \mu\text{molkg}^{-1}$) than those reported in GSS'96 and S'02 ($SEE = \pm 10.4 \mu\text{molkg}^{-1}$ and $SEE = \pm 8.7$
5 μmolkg^{-1} respectively). In general, the parameterization in S'02 overestimates the values of A_T° for
6 the Pacific Ocean with a mean bias of $15 \mu\text{molkg}^{-1}$. On the other hand, the GSS'96 equations show
7 the most disperse distribution along the $x=y$ line in Fig. 4a, mainly around the cluster of points in the
8 *AAIP* region where the alkalinity values are lower than expected ($x=y$ line). GSS'96 also
9 underestimates values of alkalinity at measured A_T° higher than $2400 \mu\text{molkg}^{-1}$.

10 The new A_T° parameterizations show a better fit in the case of the Indian Ocean (Fig. 4b). The *SEE* is
11 reduced by about 30% ($\pm 3.8 \mu\text{molkg}^{-1}$) with respect to the ones obtained for the Pacific Ocean
12 probably due to the better quality of the alkalinity measurements, which were calibrated with CRMs.
13 The reduction of the uncertainties with respect to the GSS'96 and S'99 parameterizations for the
14 Indian Ocean is also significant ($SEE = \pm 13.7 \mu\text{molkg}^{-1}$ and $SEE = \pm 6.1 \mu\text{molkg}^{-1}$ respectively).
15 The S'99 parameterization presents an average positive bias ($5.6 \mu\text{molkg}^{-1}$), while the GSS'96
16 parameterization underestimates some specific A_T° values located in the *AAIP* region, similar to what
17 happened in the case of the Pacific Ocean.

18

19 **3.2 Estimation of ΔC_{dis}**

20 The distribution of ΔC_{dis}^* obtained from equation 4 (section 2.3.2.) is shown in Figure 5a. High
21 values are located near the equator and in the California and Peru upwelling areas in the *EqP* region,
22 and also in the Arabian Sea and in the Bay of Bengal in the *EqI* region. Alternatively, relatively high
23 values are found close to the coast in the Bering Sea (*SAP*). Minimum values of ΔC_{dis}^* are located
24 mainly in the zone of the Ross Sea (*AAIP*) and relatively low values are also found in the regions of
25 the subtropical gyres (*NSTP* and *SSTIP*).

1 In a similar way to what has been done with the A_T° term, an estimation of ΔC_{dis} was calculated for
2 each region using a MLR fit ($\Delta C_{\text{dis}}^{\text{MLR}}$). Analogously to the methodology applied for the estimation of
3 A_T° , the same parameters, S , θ and PO , were introduced in the model as independent variables. The
4 $4^\circ \times 5^\circ$ grid subsurface layer data were used to obtain an empiric parameterization for each of the six
5 regions (with overlapping limits) which are shown in Table 2 together with the uncertainties of each
6 one of them and that of the whole domain. As explained before for A_T° a minor difference was also
7 found in the *SSTIP* region. The *EqP* region is the one that presents the higher ΔC_{dis} uncertainties
8 ($SEE = \pm 7.6 \mu\text{molkg}^{-1}$), however its relevance compared to the rest of considered regions is rather
9 dim given the lack of any WMF processes that occur in it. The rest of the uncertainties are rather low
10 in general, the lowest being those of the *AAIP* and *SAP* regions ($SEE = \pm 4.3 \mu\text{molkg}^{-1}$ and $SEE = \pm$
11 $5.0 \mu\text{molkg}^{-1}$ respectively), which are the most important regions in terms of WMF processes out of
12 the overall study area. For the Pacific and Indian Oceans altogether, the SEE is of $\pm 6.0 \mu\text{molkg}^{-1}$.
13 The $\Delta C_{\text{dis}}^{\text{MLR}}$ distribution looks very similar to that of ΔC_{dis}^* (Figs. 5a,b). In general, residual values are
14 randomly distributed (Fig. 5f) with the higher positive values ($\Delta C_{\text{dis}}^* \gg \Delta C_{\text{dis}}^{\text{MLR}}$) located in the *EqP*
15 region, associated with the Peru upwelling area. Negative values of the residuals have higher
16 magnitudes than the positive ones and are concentrated in specific zones of the domain that have also
17 high SEE (Table 2), namely: in the *NSTP* region ($SEE = \pm 6.1 \mu\text{molkg}^{-1}$) associated to the subtropical
18 gyre, in the *SSTIP* region ($SEE = \pm 6.1 \mu\text{molkg}^{-1}$) near South Africa (Indian Ocean) and in the *EqP*
19 region near Australia ($SEE = \pm 7.6 \mu\text{molkg}^{-1}$).
20 The works from S'02 and S'99 have also estimated ΔC_{dis}^* based on GSS'96 methodology. S'99 used
21 isopycnal surfaces to estimate ΔC_{dis}^* in the Indian Ocean but in S'02 this computation was made
22 through an Optimum MultiParameter analysis (OMP; Tomczak, 1981, Tomczak and Large, 1989) for
23 the Pacific Ocean. OMP analyses are extensively applied to determine the relative contribution
24 (mixing) of various source waters or "water types" to a water sample. Accordingly, any conservative
25 parameter measured in a water sample is the result of a linear combination of the parameter's

1 concentration from various water types that are present in the studied domain. Usually, the water
2 column is divided into several vertical layers according to the vertical distribution of the different
3 water types. S'02 applied an OMP analysis with four source waters dividing the water column into
4 four thick layers. Thus, by knowing the ΔC_{dis}^* of each water type the value of the water sample can
5 be easily deduced.

6 In order to compare with the distributions of ΔC_{dis}^* and ΔC_{dis}^{MLR} the methodologies in S'02 and S'99
7 were applied in the corresponding ocean basins, and the results are shown in Figure 5c
8 ($\Delta C_{dis}^{S99\&02}$). The distribution of $\Delta C_{dis}^{S99\&02}$ shows relatively small variability compared to ΔC_{dis}^*
9 and ΔC_{dis}^{MLR} distributions, but some different structures can be distinguished (isolines in Fig. 5c), such
10 as in case of the Southern Ocean patterns (*AAIP* region) with more negative values of disequilibrium
11 and the one associated with the upwelling regions in the Pacific Ocean (*EqP*), with low positive
12 values.

13 The atlas of pCO_2 provided by Takahashi et al. (2009) is an asset to calculate ΔC_{dis} according to
14 equation 5 (see section 2.3.2.). These pCO_2 data were downloaded and then averaged to obtain mean
15 winter values (Rodgers et al., 2008) in the Northern Hemisphere (latitude > 25 , average between
16 January and March) and Southern Hemisphere (latitude < -25 , average between July and September)
17 and the annual mean value in the Equatorial region ($-25 \leq \text{lat.} \leq 25$). The values of ΔC_{dis} (ΔC_{dis}^{TARO})
18 were calculated for the $4^\circ \times 5^\circ$ grid following equation 3 and the distribution of them is shown in
19 Figure 5d. The residuals with respect to ΔC_{dis}^* are also shown (Figs. 5e). The ΔC_{dis}^{TARO} distribution
20 (Fig. 5d) shows very similar patterns to those in the ΔC_{dis}^* distribution (Fig. 5a), with higher values
21 near the Equator and in the upwelling areas (*EqP*) and also in the Arabian Sea (*EqI*), near the Red
22 Sea outflow. Lower values appear also associated to the subtropical gyres (*NSTP* and *SSTIP*). In the
23 case of ΔC_{dis}^{TARO} , the inner Arabian Sea and the Bay of Bengal (*EqI*) do not show the higher values
24 that can be seen in ΔC_{dis}^* . The main difference between both distributions lies in the values of ΔC_{dis}
25 in the Antarctic region (*AAIP*). Values of ΔC_{dis}^{TARO} are very positive and those of ΔC_{dis}^* very negative,

1 as can be clearly seen in the residual distribution (Fig. 5e). There are also high positive values of the
 2 residuals in the *EqP* region (Peru upwelling area).
 3 For comparative examination the latitudinal variability of the different ΔC_{dis} estimations is
 4 represented for the Pacific and Indian oceans separately in Figure 6. In general, values of ΔC_{dis}^* and
 5 $\Delta C_{\text{dis}}^{\text{TARO}}$ show a clear agreement along most of the latitudinal range in both oceans except in the
 6 *AAIP* region (south of SAF). The values of ΔC_{dis}^* and $\Delta C_{\text{dis}}^{\text{MLR}}$ for the Pacific Ocean (Fig. 6a)
 7 decrease south of the SAF ($\sim 55^\circ\text{S}$; *AAIP* region), between 20°N and 40°N (southern *NSTP*) and
 8 between 20°S and 40°S (northern *SSTIP*). High values of ΔC_{dis}^* are found in the *EqP* region ($-15 < \text{lat}$
 9 < 15), in *SAP* region and in those border zones between Subtropical and Polar regions (between 40°S
 10 and 55°S in northern *NSTP* and north of 40°N in southern *SSTIP*). $\Delta C_{\text{dis}}^*_{\text{S99\&02}}$ shows only minor
 11 variability north of 40°N and south of 40°S but coincident, at least in pattern, with the other two
 12 estimations of ΔC_{dis} . The gap in the variability of $\Delta C_{\text{dis}}^*_{\text{S99\&02}}$ in temperate waters ($-40 < \text{lat} < 40$) is
 13 because of the OMP developed by S'02, which does not allow to extend $\Delta C_{\text{dis}}^*_{\text{S99\&02}}$ values for $\theta >$
 14 16°C (Table 2 in S'02). The mean differences between $\Delta C_{\text{dis}}^*_{\text{S99\&02}}$ and ΔC_{dis}^* are of $2 \pm 11 \mu\text{molkg}^{-1}$
 15 and $4 \pm 9 \mu\text{molkg}^{-1}$ for the Pacific ($n=14$) and Indian oceans ($n=10$) respectively. These values
 16 suggest that regional biases of about $10 \mu\text{molkg}^{-1}$ might be inferred in C_{ANT} estimates, which
 17 represent $\sim 20\%$ of the associated uncertainty in the computation of C_{ANT} (equation 2), taking 50
 18 μmolkg^{-1} as the mean value of C_{ANT} in upper layers. These differences are more evident in the
 19 Southern Ocean (here corresponding to the *AAIP*), where previous studies for the Atlantic Ocean
 20 have also found similar systematic discrepancies between the C_{ANT} computed from the classic ΔC^*
 21 method and those from four other methods (Lo Monaco et al., 2005; Vázquez-Rodríguez et al.,
 22 2009b).
 23 ΔC_{dis}^* and $\Delta C_{\text{dis}}^{\text{MLR}}$ show, in general, very similar variability with respect to $\Delta C_{\text{dis}}^{\text{TARO}}$ with some
 24 remarkable differences between values in points border between *EqP* region and the *NSTP* and
 25 *SSTIP* regions. In the *AAIP* region ($50\text{-}55^\circ\text{S}$ approx. in the limit of the SAF) there is a change in the

1 pattern (from negative values in ΔC_{dis}^* and $\Delta C_{\text{dis}}^{\text{MLR}}$ to positive ones in $\Delta C_{\text{dis}}^{\text{TARO}}$) and the reason of this
2 important difference between estimations lies on the different methodology applied to get the various
3 ΔC_{dis} values (equations 4 and 5), specifically due to the biological/ventilation term (AOU) accounted
4 for in equation 4 respect to equation 5.

5 In order to explain better the differences between $\Delta C_{\text{dis}}^{\text{TARO}}$ and ΔC_{dis}^* the values of AOU from the
6 surface layer are also represented. Surface AOU values were downloaded from the World Ocean
7 Atlas (WOA, http://www.nodc.noaa.gov/OC5/WOA05/pr_woa05.html), averaged to obtain winter
8 mean values and fitted into the $4^\circ \times 5^\circ$ grid in the same manner as has been done with pCO₂ data. The
9 variability of the surface averaged AOU is quite low in general showing relative moderate values (<
10 $5 \mu\text{molkg}^{-1}$) in the *EqP* and the *SAP* regions and the high values ($> 40 \mu\text{molkg}^{-1}$) in the *AAIP* region.
11 These high values correspond to zones of the ocean basin where strong and deep vertical water
12 mixing takes place (*AAIP* region) avoiding the sea surface water to reach the equilibrium with the
13 atmosphere. However, in other upwelling regions as *EqP*, *EqI* and *SAP* the mixing could be not so
14 strong involving waters from intermediate depths and leading to a small disequilibrium in the
15 concentration of O₂. Because of its implication in the estimation of ΔC_{dis}^* (equation 4), higher the
16 values of AOU are, lower the values of ΔC_{dis}^* will be obtained. The estimation of $\Delta C_{\text{dis}}^{\text{TARO}}$ does not
17 take into account the disequilibrium in the concentration of O₂ (equation 5) and the calculus results
18 in higher values of $\Delta C_{\text{dis}}^{\text{TARO}}$ with respect to ΔC_{dis}^* for these regions. Besides, the difference between
19 values of $\Delta C_{\text{dis}}^{\text{TARO}}$ and ΔC_{dis}^* are as greater as higher the values of AOU are. In order to have a
20 numerical estimation of these differences, the biological/ventilation term (computed as AOU/R_C)
21 was removed from the values of $\Delta C_{\text{dis}}^{\text{TARO}}$ ($\Delta C_{\text{dis}}^{\text{TARO}-\text{AOU}}$), the differences $\Delta C_{\text{dis}}^* - \Delta C_{\text{dis}}^{\text{TARO}}$ and $\Delta C_{\text{dis}}^* -$
22 $\Delta C_{\text{dis}}^{\text{TARO}-\text{AOU}}$ were computed and the corresponding values of the standard deviations for each of
23 these differences were obtained ($\pm 17.3 \mu\text{molkg}^{-1}$ and $\pm 11.7 \mu\text{molkg}^{-1}$ respectively). These results
24 indicate that the difference between ΔC_{dis}^* and $\Delta C_{\text{dis}}^{\text{TARO}}$ is reduced in a 32% when the
25 biological/ventilation effects are accounted for in the values of $\Delta C_{\text{dis}}^{\text{TARO}}$.

1 The latitudinal variability of the various ΔC_{dis} estimations for the Indian Ocean (Fig. 6b) is similar to
2 that of the Pacific Ocean. The better quality of the data allows for the differences between values of
3 ΔC_{dis}^* and $\Delta C_{\text{dis}}^{\text{MLR}}$ to be lower than in the case of the Pacific Ocean (Fig. 6a). The minor variability of
4 $\Delta C_{\text{dis}}^*_{\text{S99\&02}}$ is partially evident in the Indian Ocean. The lack of $\Delta C_{\text{dis}}^*_{\text{S99\&02}}$ values in the *EqI* region
5 is due to the fact that the equations for the ΔC_{dis} from S'99 are not defined for the temperature range
6 of this region and therefore cannot be applied here. Again, $\Delta C_{\text{dis}}^{\text{TARO}}$ shows much higher values with
7 respect to ΔC_{dis}^* in the *AAIP* region and the variability of AOU accounts for this difference in the
8 same way that it has been shown for the Pacific Ocean before (Fig. 6a). The standard deviation of the
9 differences between $\Delta C_{\text{dis}}^{\text{TARO}}$ and $\Delta C_{\text{dis}}^{\text{TARO-AOU}}$ with respect to ΔC_{dis}^* were of $14.3 \mu\text{molkg}^{-1}$ and 10.8
10 μmolkg^{-1} respectively, i.e., the differences between $\Delta C_{\text{dis}}^{\text{TARO-AOU}}$ and ΔC_{dis}^* are 25% lower than those
11 with respect to $\Delta C_{\text{dis}}^{\text{TARO}}$.

12

13 **4. Conclusions**

14 The main physic and chemical characteristics of each ocean and the principal zones of formation of
15 the water masses (central, intermediate and deep-bottom waters) are important features that need to
16 be taken into account in global parameterizations of A_{T}° and ΔC_{dis} . Thus, besides regionalizing the
17 domain to differentiate these oceanic features, the use of data from the subsurface layer (75-180m) is
18 needed as showing to better represent the thermohaline variability of the oceans. Furthermore, the
19 use of a grid average ($4^{\circ}\times 5^{\circ}$ grid) avoids the noise coming from the local variability and the effect of
20 having different analytical sources in the estimated values. After all these approaches, the
21 parameterizations of A_{T}° and ΔC_{dis} here obtained for the Pacific and Indian Ocean are likely to be the
22 most suitable for back-calculating C_{ANT} .

23 The obtained expressions for A_{T}° fit better and have lower uncertainties ($\pm 5.5 \mu\text{molkg}^{-1}$ and ± 3.8
24 μmolkg^{-1} for the Pacific and Indian oceans, respectively) than previous results ($\pm 10.4 \mu\text{molkg}^{-1}$ from
25 GSS'96 and $\pm 8.7 \mu\text{molkg}^{-1}$ from S'02 for the Pacific Ocean and $\pm 13.7 \mu\text{molkg}^{-1}$ from GSS'96 and

1 $\pm 6.1 \mu\text{molkg}^{-1}$ from S'99 for the Indian Ocean). The biases found in previous studies propagate into
2 current estimations of C_{ANT} and generate biases that range between 3 and $7 \mu\text{molkg}^{-1}$ stemming from
3 the computation of CaCO_3 dissolution.

4 The parameterizations obtained for ΔC_{dis} show low uncertainties in most of the regions. Remarkably,
5 the lowest uncertainties correspond to regions where the most important WMF processes occur
6 (*AAIP* and *SAP*). The ΔC_{dis}^* differences with respect to previous estimations ($\Delta C_{\text{dis}}^*_{\text{S99\&02}}$) for the
7 *AAIP* region would mean ~20% of uncertainties in the computation of C_{ANT} . There is a good
8 agreement between the values of ΔC_{dis}^* and those obtained in the base of the pCO_2 climatology
9 ($\Delta C_{\text{dis}}^{\text{TARO}}$) except for the *AAIP* region, where the effects of the low-oxygen upwelled AABW lead to
10 important biases in $\Delta C_{\text{dis}}^{\text{TARO}}$ values.

11

12

13 **ACKNOWLEDGEMENTS**

14 We would like to extend our gratitude to the chief scientists, scientists and the crew who participated
15 and put their efforts in the oceanographic cruises utilized in this study, particularly to those
16 responsible for the carbon system measurements. This study was developed and funded by the
17 European Commission within the 6th Framework Programme (EU FP6 CARBOOCEAN Integrated
18 Project, Contract no. 511176), the Spanish research project M4AO (PGIDIT07PXIB402153PR),
19 Ministerio de Educación y Ciencia (CTM2006-27116-E/MAR), Xunta de Galicia
20 (PGIDIT05PXIC40203PM), Acción Integrada Hispano-Francesa (HF2006-0094) and the French
21 research project OVIDE. Marcos Vázquez-Rodríguez was funded by Consejo Superior de
22 Investigaciones Científicas (CSIC) I3P predoctoral grant program I3P-BPD2005.

23

24

25

1 REFERENCES

- 2 Anderson, L.A., Sarmiento, J.L., 1994. Redfield ratios of remineralization determined by nutrient data
3 analysis. *Global Biogeochem. Cycles*. 8(1), 65-80.
- 4 Brewer, P.G., Goldman, J.C., 1976. Alkalinity changes generated by phytoplankton growth. *Limnology and*
5 *Oceanography*. 21, 108-117.
- 6 Brewer, P.G., 1978. Direct observation of the oceanic CO₂ increase. *Geophysical Research. Letters* 5, 997–
7 1000.
- 8 Broecker, W.S., 1974. “NO” a conservative water mass tracer. *Earth Planetary Science. Letters* 23, 8761-
9 8776.
- 10 Chen, C.T., Millero, F.J., 1979. Gradual increase of oceanic carbon dioxide. *Nature*. 277, 205–206.
- 11 Chen, C.T., Pytkowicz, R.M., 1979. On the total CO₂-titration alkalinity-oxygen system in the Pacific Ocean.
12 *Nature*. 281, 362–365.
- 13 Chen, C.T., 1990. Rates of Calcium Carbonate Dissolution and Organic Carbon Decomposition in the North
14 Pacific Ocean. *Journal of Oceanographical Society of Japan*. 46, 201–210.
- 15 Doney, S.C., Jenkins, W.J., 1988. The effect of boundary conditions on tracer estimates of thermocline
16 ventilation rates. *Jorunal of Marine Research*. 46, 947–965.
- 17 Gruber, N., Sarmiento, J.L., Stocker. T.F., 1996. An improved method for detecting anthropogenic CO₂ in the
18 oceans. *Global Biogeochemical Cycles*. 10, 809–837.
- 19 Gruber, N., Sarmiento, J.L., 1997. Global patterns of marine nitrogen fixation and denitrification. *Global*
20 *Biogeochemical Cycles*. 11, 235–266.
- 21 Gruber, N., 1998. Anthropogenic CO₂ in the Atlantic Ocean. *Global Biogeochemical Cycles*. 12, 165–191.
- 22 Key, R. M., Kozyr, A., Sabine, C. L., Lee, K., Wanninkhof, R., et al., 2004. A global ocean carbon
23 climatology: Results from Global Data Analysis Project (GLODAP). *Global Biogeochemical Cycles*.
24 18, GB4031, doi:10.1029/2004GB002247.
- 25 Körtzinger, A., Mintrop, L., Duinker, J.C., 1998. On the penetration of anthropogenic CO₂ into the North
26 Atlantic Ocean. *Journal of Geophysical Research*. 103, 18681-18689.
- 27 Le Quééré C., Raupach, M. R., Ganadell, J. G., Marladnd, G., et al., 2009. Trends in the sources and sinks of
28 carbon dioxide. *Nature Geoscience*. 2, 831-836, doi:10.1038/NGEO689.
- 29 Lo Monaco, C., Metzl, N., Poisson, A., Brunet, C., Schauer, B., 2005. Anthropogenic CO₂ in the Southern
30 Ocean: Distribution and inventory at the Indian-Atlantic Boundary (World Ocean Circulation
31 Experiment line I6). *Journal of Geophysical Research*. 110, C06010, doi:10.1029/2004JC002643.
- 32 Levine, N.M., Doney, S.C., Wanninkhof, R., Lindsay, K., Fung, I.Y., 2008. Impact of ocean carbon system
33 variability on the detection of temporal increases in anthropogenic CO₂. *Journal of Geophysical*
34 *Research*. 113, C03019, doi:10.1029/2007JC004153.
- 35 Matear, R.J., McNeil, B.I., 2003 Decadal accumulation of anthropogenic CO₂ in the Southern Ocean: A
36 comparison of CFC-age derived estimates to multiple-linear regression estimates. *Global*
37 *Biogeochemical Cycles*. 17, doi:10.1029/2003GB002089.
- 38 Matsumoto, K., Gruber, N., 2005. How accurate is the estimation of anthropogenic carbon in the ocean? An
39 evaluation of the ΔC* method. *Global Biogeochemical Cycles*. 19, doi: 10.1029/2004GB002397.
- 40 Marshall, J., Schott, F., 1999. Open-Ocean Convection: Observations, Theory, and Models. *Reviews of*
41 *Geophysics*. 37, 1-64.
- 42 Millero, F.J., Lee, K., Roche, M., 1998b. Distribution of alkalinity in the surface waters of the major oceans.
43 *Marine Chemistry*. 60, 111-130.
- 44 Pérez, F.F., Álvarez M., Ríos, A.F., 2002. Improvements on the back-calculation technique for estimating
45 anthropogenic CO₂. *Deep-Sea Research. I* 49, 859–875.
- 46 Rios, A. F., Alvarez-Salgado X. A., Pérez F. F., Bingler L. S., Arístegui J., Mémerly, L., 2003. Carbon dioxide
47 along WOCE line A14: Water masses characterization and anthropogenic entry. *Journal of*
48 *Geophysical Research*. 108(C4), 3123, doi:10.1029/2000JC000366.
- 49 Rodgers, K.B., Sarmiento, J.L., Aumont, O., Crevoisier, C., de Boyer Montégut, C., Metzl, N., 2008. A
50 wintertime uptake window for anthropogenic CO₂ in the North Pacific. *Global Biogeochemical*
51 *Cycles*. 22, doi:10.1029/2006GB002920.
- 52 Sabine, C. L., Key, R. M., Johnson, K. M., Millero, F. J. et al., 1999. Anthropogenic CO₂ inventory of the
53 Indian Ocean. *Global Biogeochemical Cycles*. 13,179–198.

- 1 Sabine, C. L., Feely, R.A., Key, R. M., Bullister, J.L., et al., 2002. Distribution of anthropogenic CO₂ in the
2 Pacific Ocean. *Global Biogeochemical Cycles*. 16, doi:10.1029/2001GB001639.
- 3 Sabine, C. L., Feely, R. A., Gruber, N., Key, R. M., et al., 2004. The Oceanic Sink for anthropogenic CO₂.
4 *Science*. 305, 367–371.
- 5 Schmitz, W. J. Jr, 1996. On the World Ocean Circulation: Volume II. Woods Hole Oceanographic Institution.
6 Technical Report. WHOI-96-08.
- 7 Takahashi, T., Sutherland, S.C., Wanninkhof, R., Sweeney, C., et al., 2009. Climatological mean and decadal
8 change in surface ocean pCO₂, and net sea-air CO₂ flux over the global oceans. *Deep-Sea Research, II*
9 56, 554-577. http://www.ldeo.columbia.edu/res/pi/CO2/carbondioxide/pages/air_sea_flux_2000.html
- 10 Thomas, H., Ittekkot, V., 2001. Determination of anthropogenic CO₂ in the North Atlantic Ocean using water
11 mass ages and CO₂ equilibrium chemistry. *Journal of Marine Systems*, 27, 325-336.
- 12 Tomczak, M., 1981. A multi-parameter extension of temperature/salinity diagram techniques for the analysis
13 of non-isopycnal mixing. *Progress in Oceanography*. 10, 147-171.
14 http://www.ldeo.columbia.edu/~jkarsten/omp_std/.
- 15 Tomczak, M., Large, D.G.B., 1989. Optimum multiparameter analysis of mixing in the thermocline of the
16 Eastern Indian Ocean. *Jorunal of Geophysical Research*. 94(C11), 16141-16149.
- 17 Tomczak, M., Godfrey, J.S., 2001. *Regional Oceanography: An Introduction*. Electronic version of 1994
18 Edition, Great Britain. <http://www.incois.gov.in/Tutor/regoc/pdfversion.html>.
- 19 Vázquez-Rodríguez, M., 2008. Reconstructing preformed properties and air-sea CO₂ disequilibria for water
20 masses in the Atlantic from subsurface data: An application in anthropogenic carbon determination.
21 Masters Thesis. University of Vigo.
22 <http://store.pangaea.de/Projects/CARBOOCEAN/MastersThesisRodriguez.pdf>.
- 23 Vázquez-Rodríguez, M., Padin, X.A., Ríos, A.F., Bellerby, R.G.J., Pérez, F. F., 2009a. An upgraded carbon-
24 based method to estimate the anthropogenic fraction of dissolved CO₂ in the Atlantic Ocean.
25 *Biogeosciences Discuss.*, 6, 4527–4571.
- 26 Vázquez-Rodríguez, M., Touratier, F., Lo Monaco, C., Waugh, D.W., Padin, X.A., et al.,
27 2009b. Anthropogenic carbon distributions in the Atlantic Ocean: databased
28 estimates from the Arctic to the Antarctic. *Biogeosciences* 6, 439 – 451.
- 29 Wallace, D.W.R., 2001. Storage and Transport of Excess CO₂ in the Oceans: The JCOFS/WOCE Global CO₂
30 Survey, in: Siedler, G., Church, W., Gould, J. (Eds.), *Ocean Circulation and Climate*. Academic Sand
31 Diego, CA. Press, pp. 489-521.
- 32 Waugh, D.W., Hall, T.M., McNeil, B.I., Key, R., Matear, R.J., 2006. Anthropogenic CO₂ in the oceans
33 estimated using transit time distributions, *Tellus*. 58B, 376-389, doi:10.1111/j.1600-
34 0889.2006.00222.x.
- 35 Woods, J.D., 1985. Physics of thermocline ventilation in: Elsevier, (Ed), *Coupled Atmosphere-Ocean Models*.
36 Nihoul, J.C.J, pp 543-590.
- 37

38

39

40

41

42

43

44

45

1
2
3
4
5
6
7
8
9
10
11
12
13
14
15
16
17
18
19
20
21
22
23
24
25

FIGURES / TABLES CAPTIONS

Figure 1: Domain, Data and Regions: a) GLODAP subsurface layer data for the whole domain; b) S distribution in the subsurface layer for the whole domain, grey dots indicate bottle data points transformed into $4^{\circ} \times 5^{\circ}$ grid; c) θ distribution in the subsurface layer for the whole domain and the names of the different regions in which the domain is divided.

Figure 2: T/S diagrams. GLODAP bottle data from 200m down (little blue circles) are represented together with computed grid data points ($4^{\circ} \times 5^{\circ}$ grid) from the first 25m (red circles) and from 75m to 180m (green circles): a) Pacific Ocean; b) Indian Ocean.

Figure 3: Distributions of alkalinity for the whole domain: a) measured alkalinity in the subsurface layer (depth range from 75m to 180m), b) computed A_T° and c) residuals (measured alkalinity minus computed A_T°) in μmolkg^{-1} .

1 Figure 4: Measured Alkalinity versus computed A_T° (MLR) in μmolkg^{-1} . Brown dots represent the
2 new parameterization computed, green dots that of GSS'96 ($A_T^\circ = 367.5 + 54.9 * S + 0.074 * PO$)
3 and blue dots that of S'02 ($A_T^\circ = 148.7 + 61.36 * S + 0.0941 * PO - 0.582 * \theta$) and S'99 ($A_T^\circ =$
4 $378.1 + 55.22 * S + 0.0716 * PO - 1.236 * \theta$): a) Pacific Ocean b) Indian Ocean.

5
6 Figure 5: Distributions of the different estimations of ΔC_{dis} in μmolkg^{-1} for the whole domain. a)
7 ΔC_{dis}^* , b) $\Delta C_{\text{dis}}^{\text{MLR}}$, c) $\Delta C_{\text{dis}}^{\text{S99\&02}}$, d) $\Delta C_{\text{dis}}^{\text{TARO}}$, e) $\Delta C_{\text{dis}}^{\text{TARO}} - \Delta C_{\text{dis}}^*$ and f) $\Delta C_{\text{dis}}^* - \Delta C_{\text{dis}}^{\text{MLR}}$.

8
9 Figure 6: Latitudinal averaged variability of ΔC_{dis}^* (black circles), $\Delta C_{\text{dis}}^{\text{MLR}}$ (grey circles), $\Delta C_{\text{dis}}^{\text{S99\&02}}$
10 (yellow triangles) and $\Delta C_{\text{dis}}^{\text{TARO}}$ (green triangles) in μmolkg^{-1} : a) Pacific Ocean and b) Indian Ocean
11 The latitudinal variability of AOU is also shown for both ocean basins (pink circles, μmolkg^{-1}).

12
13 Table 1: Limits of the six regions in which the whole domain is divided with ranges of S and θ for
14 each of them.

15
16 Table 2: Set of empiric parameterizations for A_T° and ΔC_{dis} in each region. n is the number of data
17 points and SEE accounts for the Standard Error of the Estimate. The coefficients “a” and “b” in the
18 $SSTIP$ parameterizations stand for: $a = -0.9$ and $b = -47.9$ for the Pacific Ocean, and $a = -1.6$ and $b =$
19 51.3 for the Indian Ocean.

Table(s)

[Click here to download Table\(s\): Table1.docx](#)

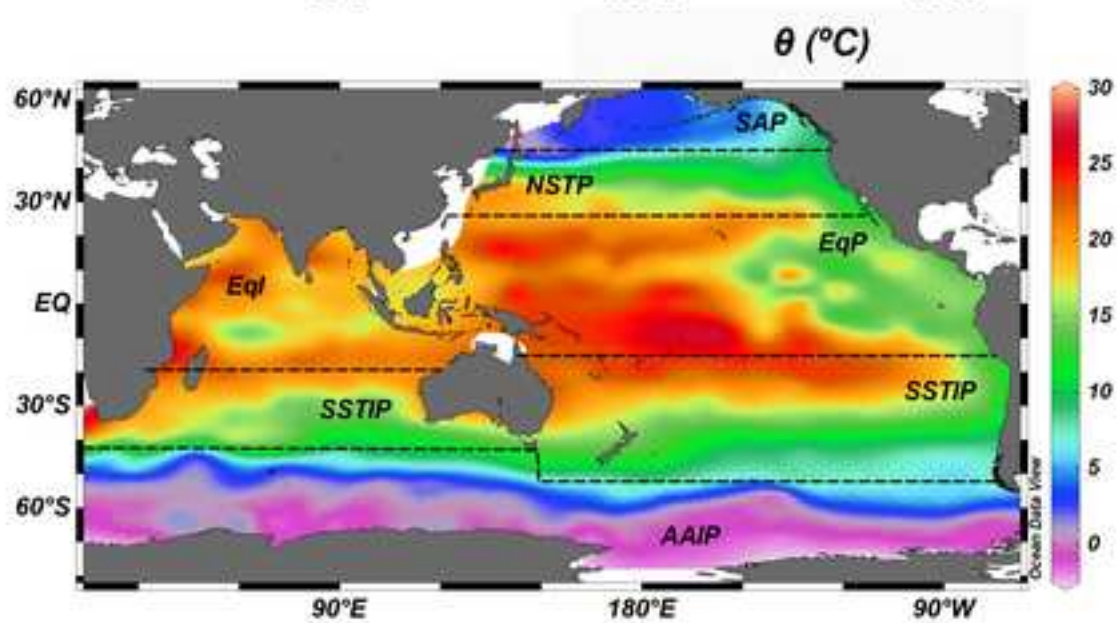
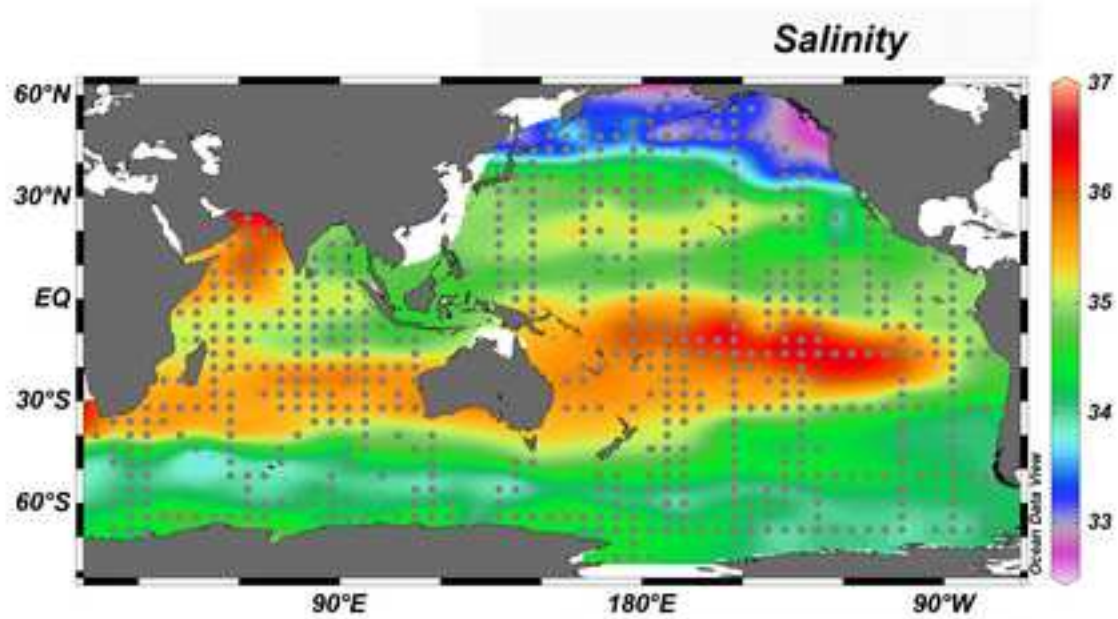
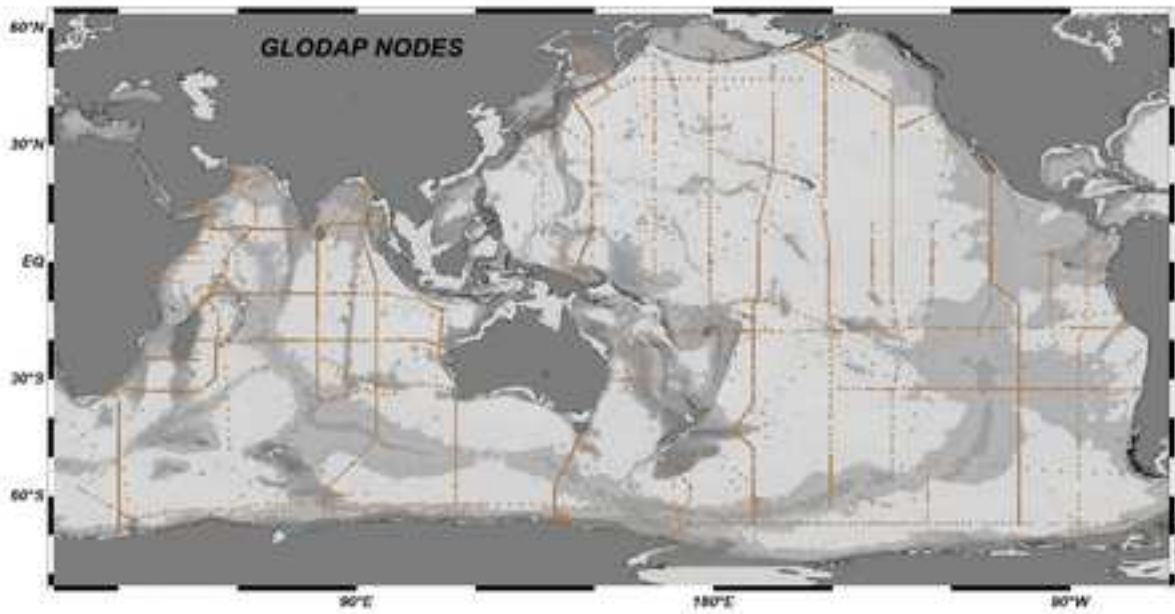
| Region | | Domain | S range | θ range (°C) |
|----------------------------------|----------------|---------------------------------|-------------|---------------------|
| <i>Subartic (SAP)</i> | | ≥ 45 | < 34.0 | < 5 |
| <i>Antarctic (AAIP)</i> | Pacific | $\leq - 54$ | 34.0 - 34.5 | < 5 |
| | Indian | $\leq - 50$ | 34.0 - 34.5 | < 5 |
| <i>Equatorial Pacific (EqP)</i> | | $- 15 \leq \text{lat.} \leq 25$ | 34.6 - 36.1 | > 20 |
| <i>North Subtropical (NSTP)</i> | | $25 < \text{lat.} < 45$ | 33.5 - 35.2 | 5 - 20 |
| <i>South Subtropical (SSTIP)</i> | Pacific | $- 54 < \text{lat.} < - 15$ | 34.2 - 36.0 | 5 - 22 |
| | Indian | $- 50 < \text{lat.} < - 25$ | 34.0 - 35.6 | 5 - 18 |
| <i>Equatorial Indian (EqI)</i> | | $\geq - 25$ | 34.9 - 36.3 | > 18 |

Table(s)

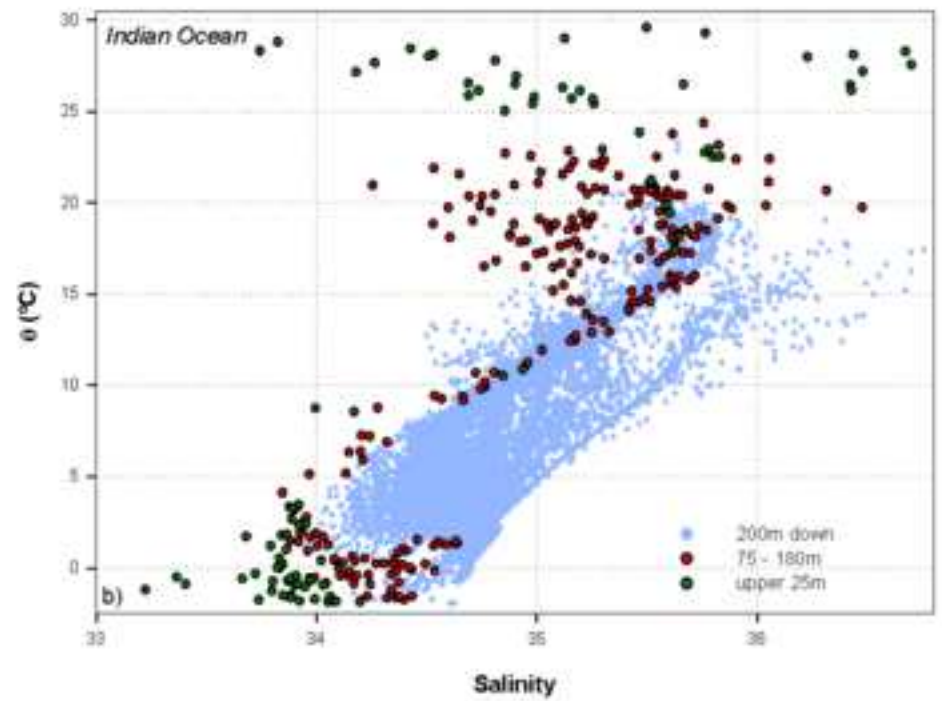
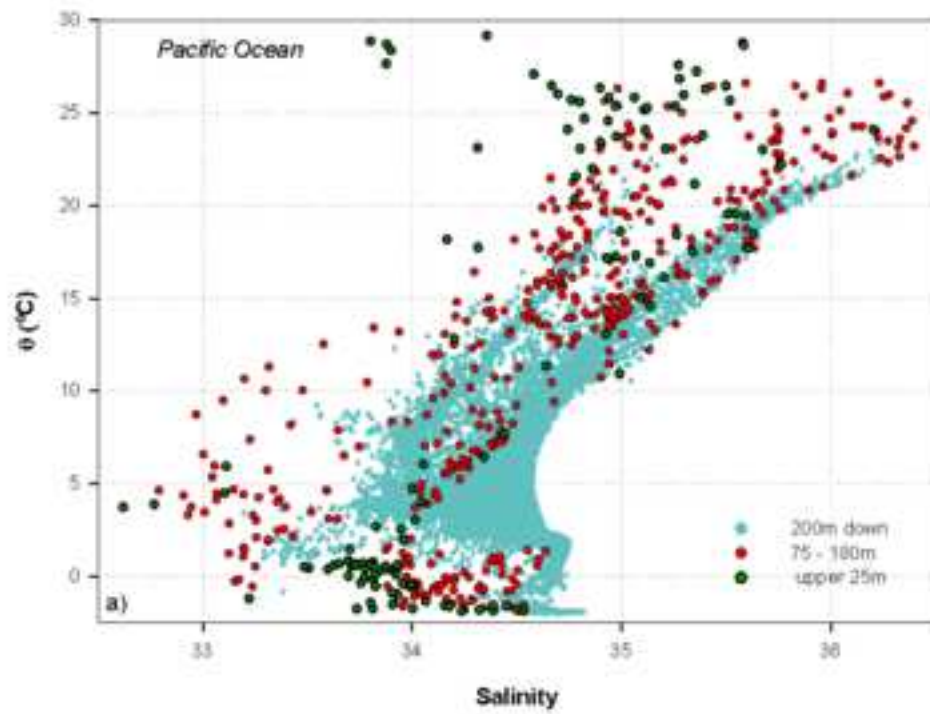
[Click here to download Table\(s\): Table2.docx](#)

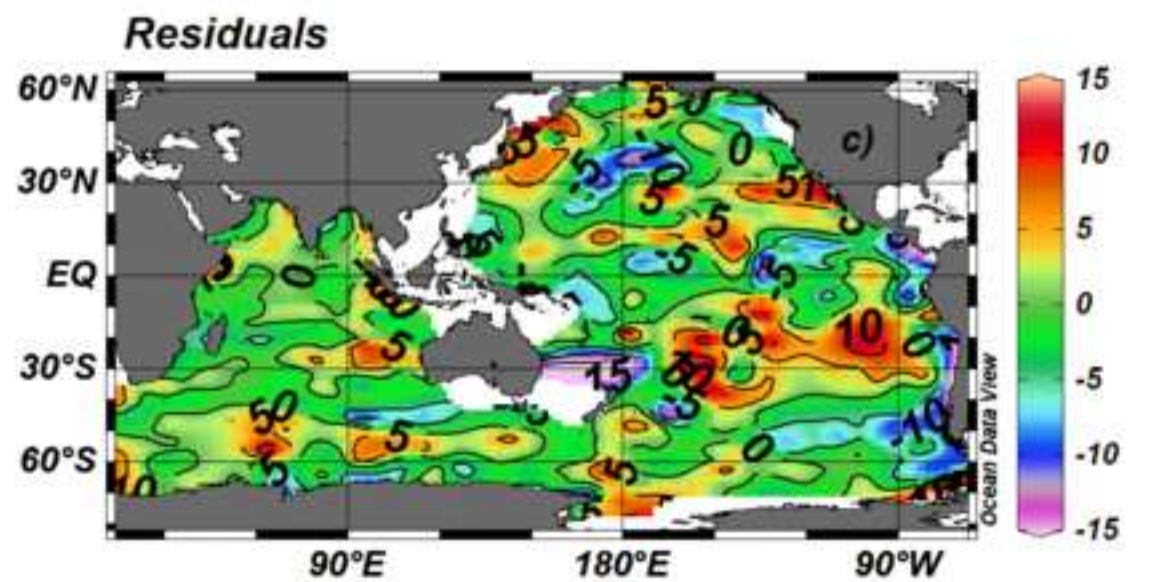
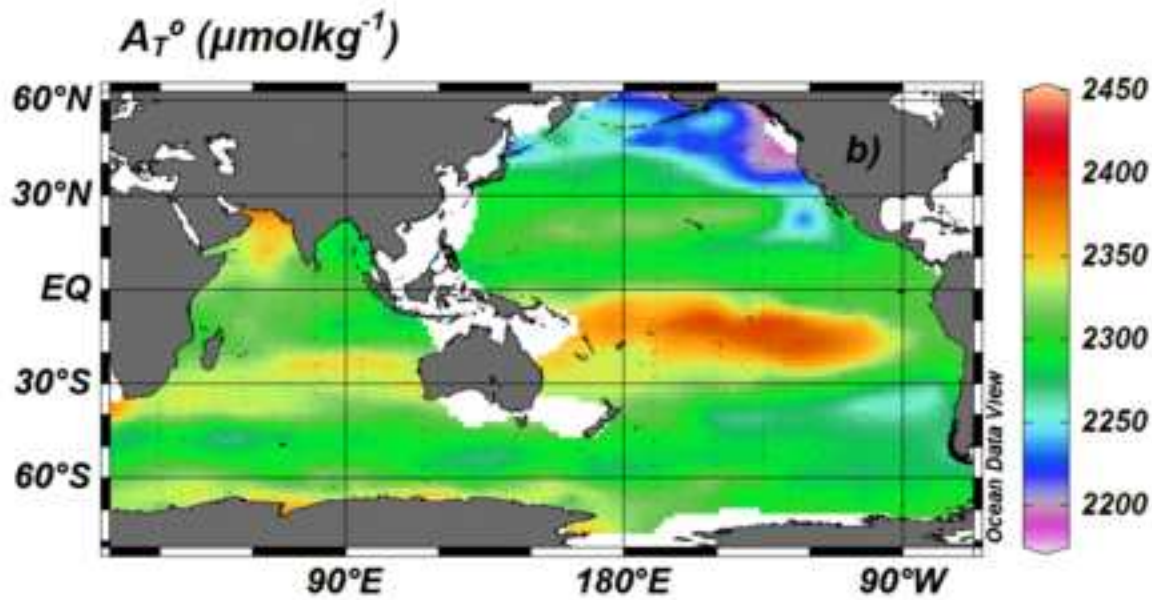
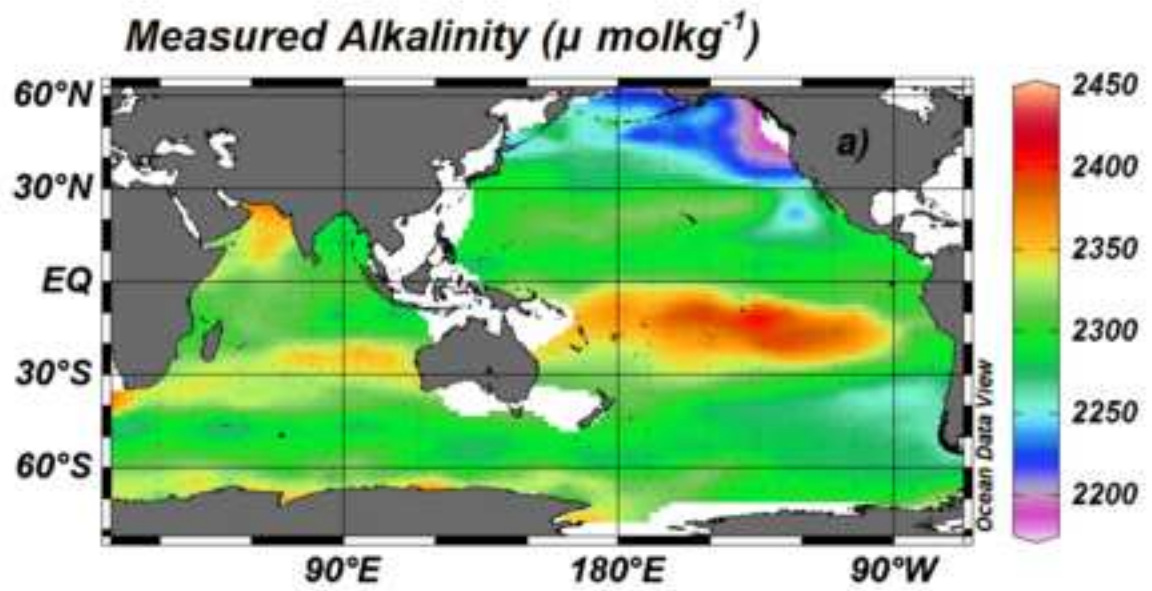
| Domain | A_T^o | ΔC_{dis} | n | SEE | |
|----------------------------------|---|--|-----|---------|------------------|
| | | | | A_T^o | ΔC_{dis} |
| <i>Subartic (SAP)</i> | $2364 + 67.1*(S-35) - 4.1*\theta + 0.04*(PO-300)$ | $-49.0 + 2.61*\theta + 0.15*(PO-300)$ | 34 | 5.0 | 5.4 |
| <i>Antarctic (AAIP)</i> | $2296.7 + 94.7*(S-35) + 0.3*(PO-300)$ | $-84.3 - 12.95*(S-35) + 5.75*\theta + 0.17*(PO-300)$ | 131 | 4.3 | 4.9 |
| <i>Equatorial Pacific (EqP)</i> | $2307.4 + 63.8*(S-35) + 0.04*(PO-300)$ | $-22.5 + 1.81*\theta + 0.18*(PO-300)$ | 133 | 5.3 | 7.6 |
| <i>North Subtropical (NSTP)</i> | $2307.9 + 61.8*(S-35) + 0.1*(PO-300)$ | $5.4 - 1.45*\theta$ | 59 | 5.9 | 6.1 |
| <i>South Subtropical (SSTIP)</i> | $2288.3 + 62.8*(S-35) - a*(\theta-16) + 0.1*(PO-300)$ | $b + 2.31*\theta + 0.16*(PO-300)$ | 185 | 6.1 | 6.4 |
| <i>Equatorial Indian (EqI)</i> | $2338 + 52.2*(S-35) - 1.9*\theta - 0.03*(PO-300)$ | $-80.2 + 4.34*\theta + 0.35*(PO-300)$ | 108 | 3.5 | 4.3 |
| Total | | | 650 | 5.2 | 6.0 |

Figure(s)
[Click here to download high resolution image](#)



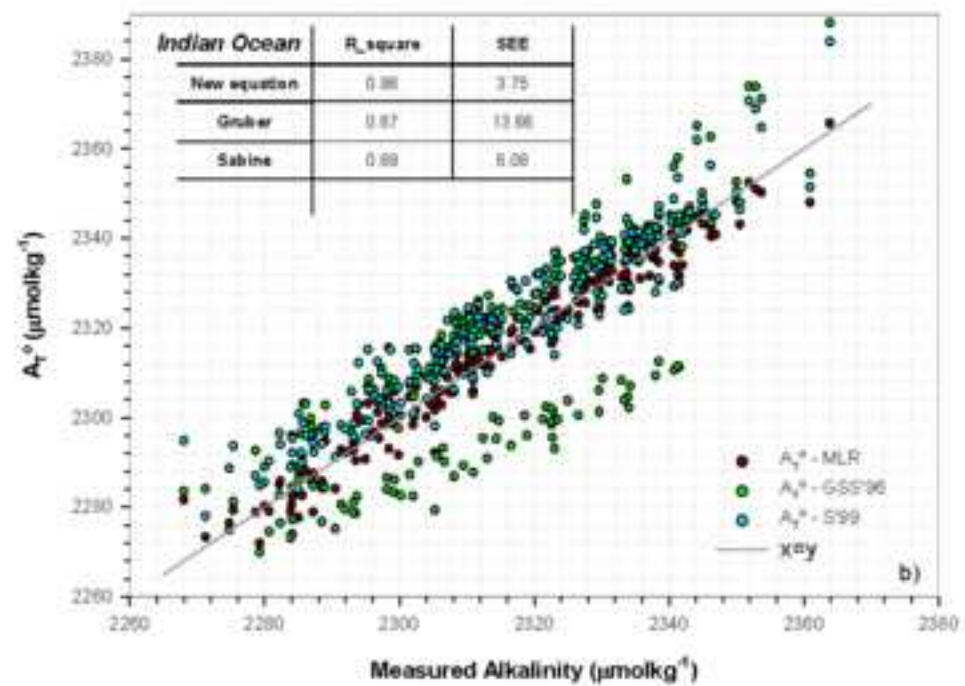
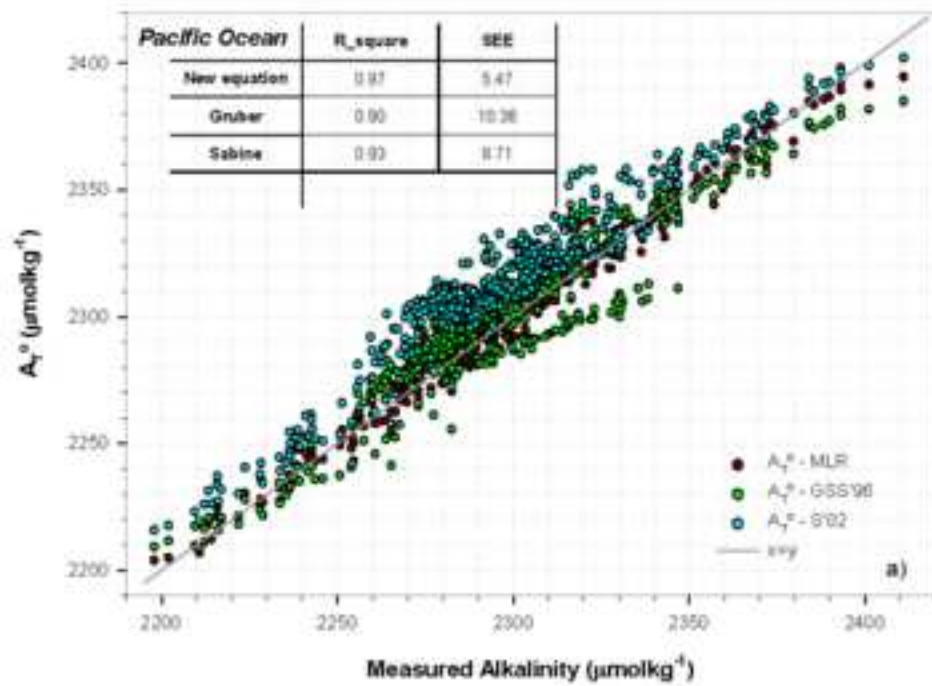
Figure(s)
[Click here to download high resolution image](#)





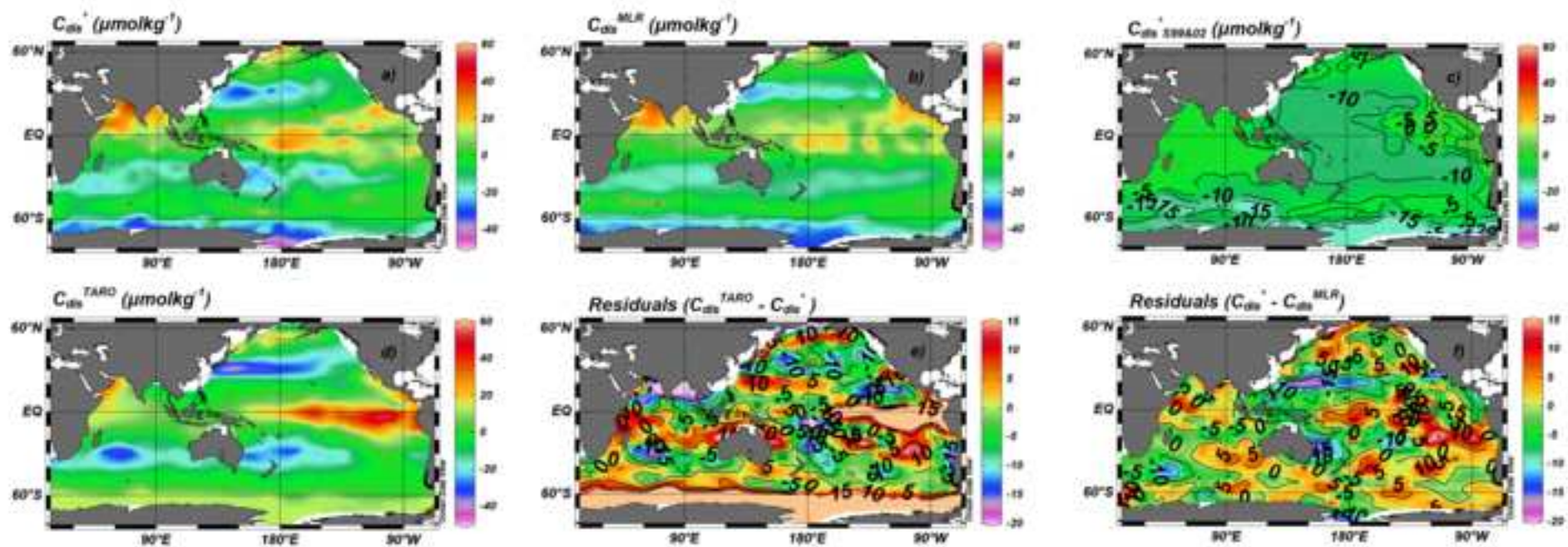
Figure(s)

[Click here to download high resolution image](#)



Figure(s)

[Click here to download high resolution image](#)



Figure(s)
[Click here to download high resolution image](#)

